

JUNO’s Impact on the Neutrino Mass Ordering from Lorentz Invariance Violation

Tatiana Araya-Santander[✉], Cesar Bonilla[✉] and Supriya Pan[✉]

*Departamento de Física, Universidad Católica del Norte,
Avenida Angamos 0610, Casillas 1280, Antofagasta, Chile*

Abstract

We explore the potential of the Jiangmen Underground Neutrino Observatory (JUNO) to probe new physics by searching for Lorentz-invariance violation (LIV). Using the 59.1-day dataset recently released by this experiment, we analyze neutrino oscillations to place new constraints on the LIV parameters in the CPT-even ($c_{ee} - c_{e\mu}$, $c_{ee} - c_{e\tau}$) and CPT-odd ($a_{ee} - a_{e\mu}$, $a_{ee} - a_{e\tau}$) sectors. Our analysis reveals a significant shift in the oscillation parameter space of $\sin^2 \theta_{12} - \Delta m_{21}^2$ when LIV is included; with the best-fit point for normal ordering moving to the higher values of the solar angle θ_{12} , a strong preference emerges for inverted mass ordering. In particular, the $c_{ee} - c_{e\tau}$ and $a_{ee} - a_{e\tau}$ sectors show the most pronounced effects. We report the most stringent bounds from JUNO to date on these LIV parameters, showcasing the detector’s unique sensitivity to physics beyond the Standard Model.

1 Introduction

The Standard Model (SM) describes most known interactions in particle physics, but it still cannot explain several important observations. A prominent example is neutrino oscillation, which demonstrates that neutrinos possess non-zero masses and undergo flavor mixing—features absent in the minimal formulation of the SM. In the three-flavor framework, neutrino propagation in vacuum leads to oscillation probabilities of the form [1]

^{*}E-mail: tatiana.araya@alumnos.ucn.cl

[†]E-mail: cesar.bonilla@ucn.cl

[‡]E-mail: supriya.pan@ucn.cl

$$\begin{aligned}
P_{\nu_\alpha \rightarrow \nu_\beta}(L, E) &= \delta_{\alpha\beta} - 4 \sum_{i>j} \operatorname{Re} \left(U_{\alpha i}^* U_{\beta i} U_{\alpha j} U_{\beta j}^* \right) \sin^2 \left(\frac{\Delta m_{ij}^2 L}{4E} \right) \\
&+ 2 \sum_{i>j} \operatorname{Im} \left(U_{\alpha i}^* U_{\beta i} U_{\alpha j} U_{\beta j}^* \right) \sin \left(\frac{\Delta m_{ij}^2 L}{2E} \right), \tag{1}
\end{aligned}$$

where $U_{\alpha i}$ are the elements of the Pontecorvo-Maki-Nakagawa-Sakata (PMNS) mixing matrix, $\Delta m_{ij}^2 \equiv m_i^2 - m_j^2$ denotes the mass-squared differences, L is the distance between the source and detector, and E is the neutrino energy.

The PMNS matrix is parameterized by three mixing angles ($\theta_{12}, \theta_{13}, \theta_{23}$), a Dirac CP-violating phase δ_{CP} , and -if neutrinos are Majorana particles- two additional Majorana phases that do not affect oscillation probabilities. Oscillations are thus governed by these three mixing angles, two independent mass-squared differences ($\Delta m_{21}^2, \Delta m_{31}^2$), and δ_{CP} .

While $\theta_{12}, \theta_{13}, \Delta m_{21}^2$, and $|\Delta m_{31}^2|$ are known with good precision, several fundamental questions remain. They are, the value of δ_{CP} , the octant of θ_{23} , and the sign of Δm_{31}^2 , which defines the neutrino mass ordering. The normal ordering (NO) corresponds to $m_3 > m_2 > m_1$, whereas the inverted ordering (IO) implies $m_2 > m_1 > m_3$. Addressing these questions, along with determining the Dirac/Majorana nature of neutrinos and their absolute mass scale, drives current experimental efforts worldwide, utilizing neutrinos from radioactive elements (Xenon-136, Germanium-76, Calcium-48), accelerator beams, nuclear reactors, as well as atmospheric, solar, and astrophysical neutrinos.

Experimental sensitivity to oscillation parameters is governed by the ratio L/E , which determines the oscillation frequency. Reactor antineutrino experiments, operating at MeV-scale energies with baselines from $\mathcal{O}(10)$ to $\mathcal{O}(10^5)$ meters [1], are particularly sensitive to $\theta_{12}, \theta_{13}, \Delta m_{21}^2$, and Δm_{31}^2 through precise measurements of the $\bar{\nu}_e$ survival probability.

The Jiangmen Underground Neutrino Observatory (JUNO) exemplifies this approach as a next-generation, high-precision reactor neutrino experiment. With excellent energy resolution and background rejection capabilities, JUNO aims to precisely measure solar parameters and determine the neutrino mass ordering (MO). Although its initial 59.1-day dataset is insufficient for a MO determination, it already provides the world's most precise constraints: $\sin^2 \theta_{12} = 0.3092 \pm 0.0087$ and $\Delta m_{21}^2 = (7.50 \pm 0.12) \times 10^{-5}$ eV² (assuming NO) [2].

This high precision also makes JUNO an ideal facility for probing subleading effects from new physics beyond the SM. In this work, we explore JUNO's sensitivity to Lorentz invariance violation (LIV). Lorentz invariance underpins the isotropy and homogeneity of local relativistic quantum field theories, including the minimal SM. Its violation would signal that the SM is a low-energy limit of a more fundamental theory. We compute JUNO's sensitivity to both CP-conserving and CP-violating LIV scenarios using its initial data release.

Several neutrino experiments have previously examined LIV effects. Constraints on LIV parameters have been obtained from accelerator [3–11], atmospheric [12, 13], and solar neutrino data [14]. More recently, reactor neutrino oscillations have also been investigated in

the context of LIV [15]. Additional studies have considered LIV in the interpretation of high-energy astrophysical neutrino events, particularly the event KM3-230213A observed at KM3NeT [16–18], as well as in neutrinoless double-beta decay experiments [19, 20]. Our work extends this program by performing a dedicated analysis of JUNO’s capabilities to constrain CPT-even LIV coefficients using its recently released real data.

This article is organized as follows. Section 2 outlines the theoretical framework for Lorentz invariance violation within neutrino oscillations. Section 3 provides a description of the JUNO experiment, its capabilities relevant to this analysis, and details our numerical methodology and statistical procedures. The resulting constraints on LIV parameters and their physical implications are discussed in Section 4. Our conclusions are presented in Section 5.

2 Lorentz Invariance Violation in Neutrino Oscillation

Following the motivation outlined in the Introduction, we present the theoretical framework for Lorentz invariance violation (LIV) in neutrino oscillations. While the standard three-flavor oscillation paradigm successfully explains a wide range of experimental data, several unresolved anomalies and theoretical considerations motivate the search for new physics beyond this minimal framework [21]. In particular, Planck-scale physics ($m_P \simeq 10^{19}$ GeV) could induce tiny low-energy violations of fundamental symmetries, such as Lorentz invariance, which might be accessible in precision neutrino experiments.

A general approach to parameterizing Lorentz and CPT violation is provided by an extension of the SM that incorporates fixed background tensor fields. These background fields couple to SM fields, inducing subtle deviations from standard particle behavior that may become observable in high-precision experiments. Within the neutrino sector, this SM extension modifies the propagation Hamiltonian by including additional terms in the Lagrangian. The contribution of these terms to the effective neutrino Hamiltonian, at leading order, is parameterized as [22, 23]

$$\mathcal{L}_{\text{LIV}} \supset -(a_L)_\mu \bar{\psi} \gamma^\mu \psi + \frac{1}{2} i(c_L)_{\mu\nu} \bar{\psi} \gamma^\mu \overset{\leftrightarrow}{D}^\nu \psi + \dots, \quad (2)$$

where $(a_L)_\mu$ and $(c_L)_{\mu\nu}$ are matrices in flavor space. The coefficients $(a_L)_\mu$ are CPT-odd and therefore break both CPT and Lorentz invariance, while the coefficients $(c_L)_{\nu\mu}$ are CPT-even and break Lorentz invariance but preserve CPT. When applied to neutrinos, the leading contributions from these operators take the form

$$\mathcal{L}_{\text{eff}}^\nu = \mathcal{L}_{\text{SM}}^\nu - (a_L)_{\alpha\beta}^\mu \bar{\nu}_\alpha \gamma^\mu \nu_\beta + \frac{1}{2} i(c_L)_{\alpha\beta}^{\mu\nu} \bar{\nu}_\alpha \gamma_\mu \overset{\leftrightarrow}{\partial}_\nu \nu_\beta, \quad (3)$$

where Greek indices label flavor. These terms modify neutrino propagation by introducing new contributions to the effective Hamiltonian. Including standard vacuum oscillations and matter effects, the full Hamiltonian relevant for oscillations is as follows,

$$H_{\text{eff}} = H_0 + H_{\text{MSW}} + H_{\text{LIV}}, \quad (4)$$

where H_{MSW} is the contribution due to standard matter interactions, and H_{LIV} stands for LIV contribution given by

$$\begin{aligned} H_{\text{LIV}} &= (a_L)_{\alpha\beta} - \frac{4}{3}E_\nu(c_L)_{\alpha\beta} \\ &= \begin{bmatrix} a_{ee} & a_{e\mu} & a_{e\tau} \\ a_{e\mu}^* & a_{\mu\mu} & a_{\mu\tau} \\ a_{e\tau}^* & a_{\mu\tau}^* & a_{\tau\tau} \end{bmatrix} - \frac{4}{3}E_\nu \begin{bmatrix} c_{ee} & c_{e\mu} & c_{e\tau} \\ c_{e\mu}^* & c_{\mu\mu} & c_{\mu\tau} \\ c_{e\tau}^* & c_{\mu\tau}^* & c_{\tau\tau} \end{bmatrix}. \end{aligned} \quad (5)$$

The factor $-4/3$ appears because the trace component of (c_L) is not observable in oscillation experiments [24]. The key feature of (5) is the distinct energy dependence of the two terms: CPT-odd coefficients a_L produce energy-independent shifts to the Hamiltonian, whereas CPT-even coefficients c_L introduce corrections that grow linearly with the neutrino energy. As a result, different types of experiments—reactor, solar, atmospheric, and accelerator—are sensitive to different combinations of SME parameters.

The sensitivity to Lorentz-violating effects depends not only on the size of the SME coefficients but also on how well an experiment can detect small changes in the oscillation pattern. High statistics, excellent energy resolution, and well-controlled systematics are therefore important for probing sub-leading LIV effects. Medium-baseline reactor experiments offer a clean environment for such studies. In the next section, we introduce the JUNO experiment and describe the features that make it well suited for testing both standard oscillation physics and potential Lorentz-violating effects.

3 JUNO: Experimental Setup and Analysis

The Jiangmen Underground Neutrino Observatory (JUNO) is a multi-purpose medium-baseline neutrino experiment located in China. It consists of a 20 k-ton liquid scintillator detector situated about 52.5 km from the Yangjiang and Taishan nuclear power plants. The primary goal of JUNO is to determine the neutrino MO with a significance of $3\text{-}4\sigma$ by measuring the energy spectrum of reactor antineutrinos with unprecedented precision [25]. The medium baseline was chosen because the survival probability of electron antineutrinos is minimal. In addition to this main objective, JUNO will also provide precise measurements of several neutrino mixing parameters and contribute to searches for physics beyond the Standard Model.

JUNO is capable of observing a wide range of neutrino sources, including solar, atmospheric, geoneutrinos, and supernova neutrinos. Reactor antineutrinos are primarily detected through the inverse beta decay processes,

$$\bar{\nu}_e + p \rightarrow e^+ + n. \quad (6)$$

The first signal (prompt) in the detector is a scintillation signature left by the positron e^+ and its annihilation, producing two gamma rays of $E_\gamma = 0.511$ MeV. Then there is a second gamma signal (delayed) coming from neutron n capture of $E_\gamma = 2.223$ MeV. The prompt and delayed signals are linked by $200\ \mu\text{s}$, which acts as a veto to reject backgrounds. The neutrino energy E_ν is linked to prompt energy E_{prompt} as $E_\nu \simeq E_{\text{prompt}} + 0.78$ MeV.

It is expected that JUNO will measure the two solar parameters, Δm_{21}^2 and $\sin^2 \theta_{12}$, as well as the atmospheric mass splitting Δm_{31}^2 , after six years of data-taking.

Using (1) the reactor antineutrino survival probability in vacuum is given by

$$P_{\bar{\nu}_e \rightarrow \bar{\nu}_e} = 1 - \cos^2 \theta_{13} \sin^2 2\theta_{12} \sin^2 \left(\frac{\Delta m_{21}^2 L}{4E} \right) - \sin^2 2\theta_{13} \left[\cos^2 \theta_{12} \sin^2 \left(\frac{\Delta m_{31}^2 L}{4E} \right) + \sin^2 \theta_{12} \sin^2 \left(\frac{\Delta m_{32}^2 L}{4E} \right) \right], \quad (7)$$

where $\Delta m_{ij}^2 \equiv m_i^2 - m_j^2$ is the squared neutrino mass difference, L the source-detector distance, and E is the neutrino energy.

The first term, proportional to Δm_{21}^2 and θ_{21} , corresponds to the ‘solar’ oscillation. It has a long oscillation length and produces a wide valley in the probability. The second term, driven by Δm_{31}^2 and θ_{13} , generates oscillations with a much shorter period (‘rapid oscillations’) and appears as small ripples superimposed on that valley [25].

In presence of LIV the reactor antineutrino survival probability becomes [15]

$$P_{\bar{\nu}_e \rightarrow \bar{\nu}_e} = 1 - \cos^2 \theta_{13} \sin^2 2\theta_{12} \sin^2 \left(\frac{\Delta m_{21}^2 L}{4E} + f_{21} \right) - \sin^2 2\theta_{13} \left[\cos^2 \theta_{12} \sin^2 \left(\frac{\Delta m_{31}^2 L}{4E} + f_{31} \right) + \sin^2 \theta_{12} \sin^2 \left(\frac{\Delta m_{32}^2 L}{4E} + f_{31} \right) \right], \quad (8)$$

where the frequencies f_{ij} (with $i, j = 1, 2, 3$) are defined in [15].

Notice that, the oscillation probability in (7) changes in presence of LIV leading to (8), where the oscillation frequencies are modified by the LIV dependent parameters f_{21} and f_{31} [15]. As the experimental data depend on these oscillation frequencies, the input of LIV can impact the fit of the data through f_{21} and f_{31} . However, this analytical formula of probability is not used in our numerical analysis. To assess JUNO’s sensitivity to LIV effects, we perform a quantitative study using the recently released 59.1-day data set [25]. The simulations are carried out with the GLoBES framework [26–28], which we modify to include the LIV Hamiltonian described in Section 2.

The statistical analysis follows the standard χ^2 formalism with pull terms. The total χ^2

is obtained after marginalization over the oscillation parameters ω and the systematic pull variables ξ as follows

$$\Delta\chi^2 = \min \left[\chi_{\text{stat}}^2(\omega, \xi) + \chi_{\text{pull}}^2(\xi) \right]. \quad (9)$$

The Poissonian statistical contribution is defined as

$$\chi_{\text{stat}}^2(\omega, \xi) = 2 \sum_i \left[N_i^{\text{test}} - N_i^{\text{true}} + N_i^{\text{true}} \ln \left(\frac{N_i^{\text{true}}}{N_i^{\text{test}}} \right) \right], \quad (10)$$

while the pull term encoding systematic uncertainties is

$$\chi_{\text{pull}}^2 = \sum_{r=1}^4 \xi_r^2. \quad (11)$$

Here, N_i^{true} denotes the observed number of events in the i th JUNO energy bin of the 59.1 days dataset, and N_i^{test} represents the predicted event obtained from the theoretical model under test (GLoBES). The ranges over which the oscillation and LIV parameters are varied are listed in Table 1.

Parameter	Variation range
θ_{12}	$[30.0^\circ, 36.1^\circ]$
θ_{13}	$[8.3^\circ, 8.6^\circ]$
Δm_{21}^2	$[7.1, 8.1] \times 10^{-5} \text{ eV}^2$
Δm_{31}^2	$[2.4, 2.5] \times 10^{-3} \text{ eV}^2$

Table 1: Variation ranges of oscillation parameters used in the analysis. Parameters θ_{23} and δ_{CP} do not affect the reactor antineutrino oscillation probability and are therefore not varied. We are using the current bounds on θ_{13} and Δm_{31}^2 from the Daya Bay experiment [29].

In our analysis, we have first normalized the unoscillated events obtained from GLoBES to the unoscillated events shown by the black dotted curve on the left and dark blue curve on the right of Figure 1, respectively. The N_i^{true} is taken from the JUNO data. We then simulated the oscillated events, including LIV, using GLoBES for N_i^{test} . The analysis uses 64 prompt-energy bins spanning the range E_{prompt} in $[1, 9]$ MeV. We assume a baseline of 52.5 km, corresponding to the reactor–detector distance, and adopt an energy resolution of 3% for all energies.

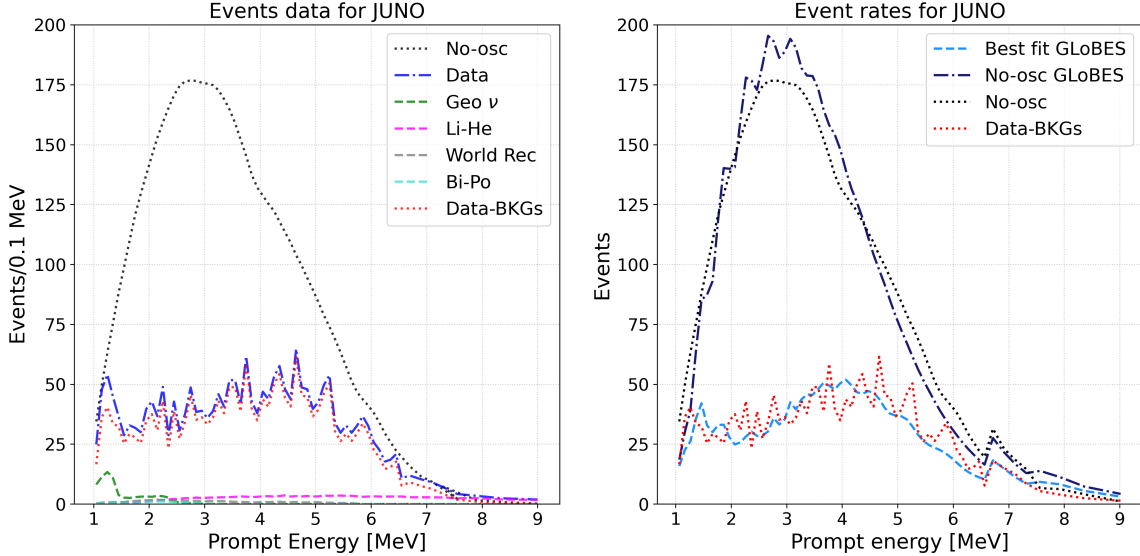


Figure 1: Left: Reconstructed JUNO prompt energy spectrum (per 0.1 MeV) from 59.1 day data set [2]. The blue curve shows the raw experimental data, while the red curve represents the data after subtracting all background components, shown individually as the green ($\text{geo-}\nu$), pink (${}^9\text{Li}/{}^8\text{He}$), grey (world reactors), and light blue (${}^{214}\text{Bi}-{}^{214}\text{Po}$) contributions. The black dotted curve represents the expected unoscillated reactor flux. Right: Unoscillated event rates from JUNO (black) compared with GLoBES simulations (dark blue). The events using the best-fit obtained using GLoBES prediction for standard oscillation for NO are shown in light blue. The experimental events after subtracting all the backgrounds from JUNO data (blue) are shown by the red curve in both panels. These comparisons validate the input used for the LIV sensitivity analysis.

4 Results

We have, to start with, compared the JUNO data with the SM events obtained through GLoBES. We have plotted the sensitivity ($\Delta\chi^2$) in the $\sin^2\theta_{12} - \Delta m_{21}^2$ plane as in [2].

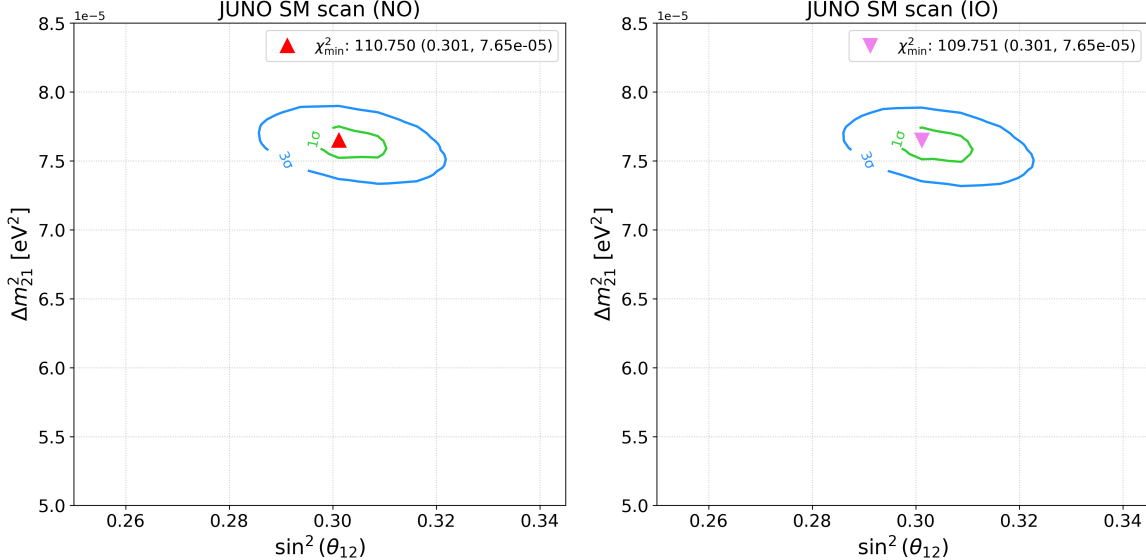


Figure 2: Total chi-square for $\sin^2 \theta_{12} - \Delta m_{21}^2$ plane for NO (left) and IO (right). 1σ and 3σ contours are shown by green and blue lines, respectively, along with the best-fit point. This χ^2 analysis was computed marginalizing on Δm_{31}^2 and θ_{13} parameters.

We determined the sensitivity to the remaining solar parameters (θ_{12} and Δm_{21}^2) by marginalizing over θ_{13} and Δm_{31}^2 , as detailed in Table 1, considering both Normal Ordering (NO) and Inverted Ordering (IO). The resulting χ^2 surface and confidence regions in the $(\Delta m_{21}^2, \sin^2 \theta_{12})$ plane are shown in Figure 2. The minimum χ^2 values reveal that the IO provides a slightly better fit to the JUNO data, with $\chi_{\min}^2 = 109.751$ (violet triangle), compared to $\chi_{\min}^2 = 110.750$ for the NO (red triangle). This results in a $\Delta\chi_{\text{NO-IO}}^2 = 0.999$ preference for IO. Furthermore, the best-fit and 3σ regions obtained in our analysis are similar to those presented in [2], whose best-fit point is located within our 1σ region.

We now examine the sensitivity of JUNO data to LIV effects. First, we consider CP-conserving, energy-dependent parameters, as defined in (5).

The sensitivity is explored through two-dimensional projections of the LIV parameter space. The analysis assumes normal ordering, with comparable results for inverted ordering shown in Appendix A. In all following scenarios, we have marginalized all standard oscillation parameters as listed in Table 1.

In Figure 3, the sensitivity in $c_{ee} - c_{e\mu}$ and $c_{ee} - c_{e\tau}$ plane has been depicted in the left and right panels, respectively, while varying them in the range $(10^{-22}, 10^{-18})$. The main observations can be summarized as follows,

- In the $c_{ee} - c_{e\mu}$ plane (left panel), values larger than $c_{ee} > 3.7 \times 10^{-19}$ and $c_{e\mu} > 0.7 \times 10^{-19}$ are excluded at the 3σ confidence level. The best-fit point is found at $c_{ee} \simeq 1.78 \times 10^{-19}$ and $c_{e\mu} \simeq 0.01 \times 10^{-19}$, yielding $\chi^2 = 110.702$, which slightly improves compared to the SM minimum $\chi_{\min}^2 = 110.750$.

- In the presence of the $c_{ee} - c_{e\tau}$ coefficients (right panel), the data discards values larger than $c_{ee} > 4.25 \times 10^{-19}$ and $c_{e\tau} > 1.03 \times 10^{-19}$ at the 3σ confidence level. The best-fit point is obtained at $c_{ee} \simeq 2.85 \times 10^{-19}$, $c_{e\tau} \simeq 0.13 \times 10^{-19}$ with $\chi^2 = 110.319$ that is less than standard $\chi^2_{\min} = 110.750$.

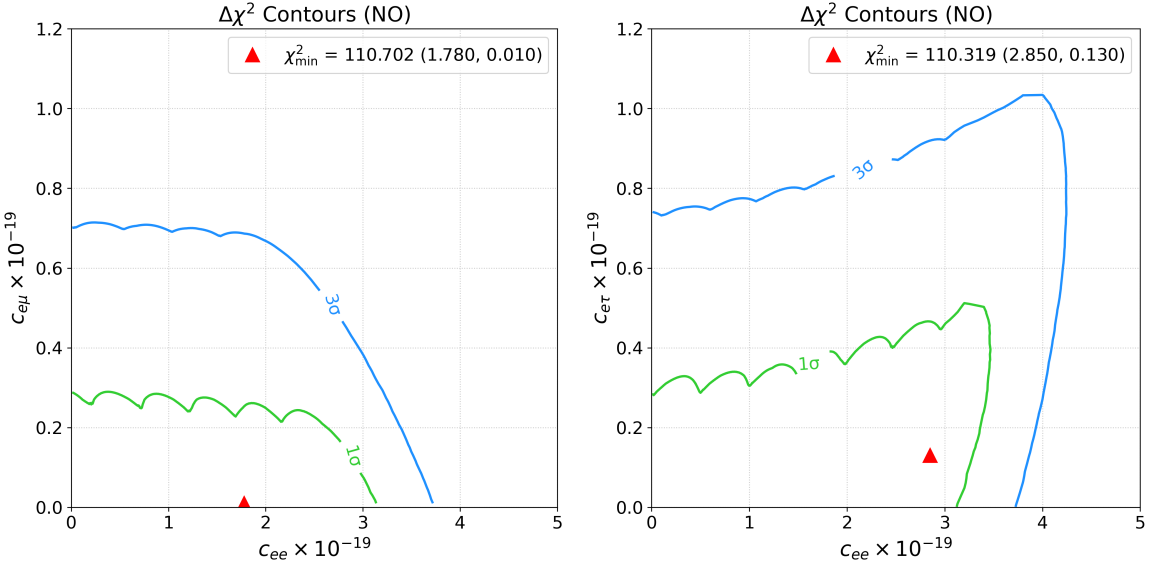


Figure 3: Two dimensional $\Delta\chi^2$ contours for the LIV parameter pairs $(c_{ee}, c_{e\mu})$ (left) and $(c_{ee}, c_{e\tau})$ (right) assuming normal ordering. The red triangles mark the global minima of each scan, which correspond to the best-fit LIV values preferred by the data. 1σ and 3σ contours are shown by green and blue lines, respectively.

The sensitivity to the LIV parameters is shown in Figure 4, with the $c_{e\mu}-\phi_{e\mu}$ plane displayed in the left panel and the $c_{e\tau}-\phi_{e\tau}$ plane in the right panel. The main observations are:

- The sensitivity in LIV phases $\phi_{e\mu}, \phi_{e\tau}$ are poor as we do not obtain a close contour.
- But around $\pi/2, 3\pi/2$ values of phases, the sensitivity in corresponding LIV parameters becomes worse as seen from the larger 3σ contours around these values. The 3σ bounds are $c_{e\mu} \simeq 3.3 \times 10^{-19}$, and $c_{e\tau} \simeq 3.1 \times 10^{-19}$.
- The best-fit values for left panel is $c_{e\mu} \simeq 0.77 \times 10^{-19}, \phi_{e\mu} = \pi/2$, while in right panel it is $c_{e\tau} \simeq 0.76 \times 10^{-19}, \phi_{e\tau} = \pi/2$ with $\chi^2 = 110.56$.

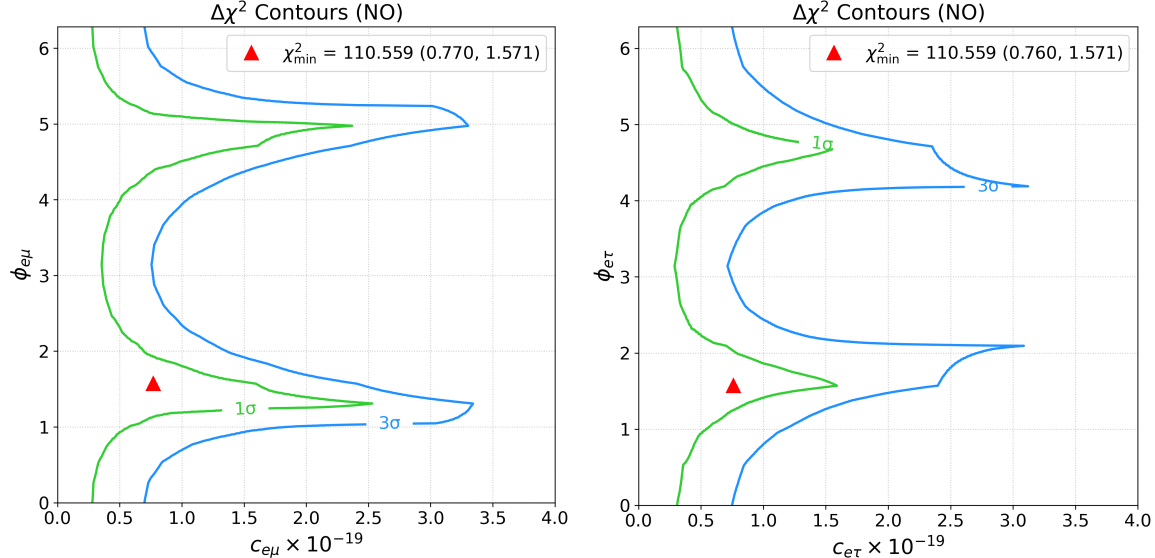


Figure 4: Two dimensional $\Delta\chi^2$ contours for the LIV parameter pairs $(c_{e\mu}, \phi_{e\mu})$ (left) and $(c_{e\tau}, \phi_{e\tau})$ (right) assuming normal ordering. The red triangles mark the global minima of each scan, which correspond to the best-fit LIV values preferred by the data. 1σ and 3σ contours are shown by green and blue lines, respectively.

Plane	$c_{ee} - c_{e\mu}$	$c_{ee} - c_{e\tau}$	$c_{e\mu} - \phi_{e\mu}$	$c_{e\tau} - \phi_{e\tau}$
Best Fit	$(1.78, 0.01) \times 10^{-19}$	$(2.85, 0.13) \times 10^{-19}$	$(0.77 \times 10^{-19}, 1.57)$	$(0.76 \times 10^{-19}, 1.57)$
χ^2_{\min}	110.70	110.319	110.56	110.56
3σ	$(3.7, 0.7) \times 10^{-19}$	$(4.25, 1.03) \times 10^{-19}$	$(3.3 \times 10^{-19}, \text{N.A.}^1)$	$(3.1 \times 10^{-19}, \text{N.A.}^1)$

¹ The whole range is allowed.

Table 2: The best-fit values, χ^2_{\min} at the best-fit and 3σ bounds in our analysis (Fig. 3) for NO. A marginalization was performed on the parameter $\theta_{12}, \theta_{13}, \Delta m_{21}^2$ and Δm_{31}^2 .

Plane	$c_{ee} - c_{e\mu}$	$c_{ee} - c_{e\tau}$	$c_{e\mu} - \phi_{e\mu}$	$c_{e\tau} - \phi_{e\tau}$
Best Fit	$(0.01, 0.01) \times 10^{-19}$	$(0.01, 0.05) \times 10^{-19}$	$(0.73 \times 10^{-19}, 1.57)$	$(0.72 \times 10^{-19}, 1.57)$
χ^2_{\min}	109.80	109.55	109.48	109.48
3σ	$(3.7, 0.7) \times 10^{-19}$	$(4.13, 0.95) \times 10^{-19}$	$(3.3 \times 10^{-19}, \text{N.A.}^1)$	$(3.05 \times 10^{-19}, \text{N.A.}^1)$

¹ The whole range is allowed.

Table 3: The best-fit values, χ^2_{\min} at the best-fit and 3σ bounds in our analysis (Fig. 9) for IO. A marginalization was performed on the parameter $\theta_{12}, \theta_{13}, \Delta m_{21}^2$ and Δm_{31}^2 .

Using these best-fit LIV coefficients as fixed inputs, we generate JUNO+LIV sensitivity contours in the Δm_{21}^2 – $\sin^2 \theta_{12}$ plane, marginalizing over θ_{13} and Δm_{31}^2 within the ranges given in Table 1. Figure 5 shows these contours for both NO and IO, in the presence of the best-fit LIV parameters $(c_{ee}, c_{e\mu})$ (left panel) and $(c_{ee}, c_{e\tau})$ (right panel).

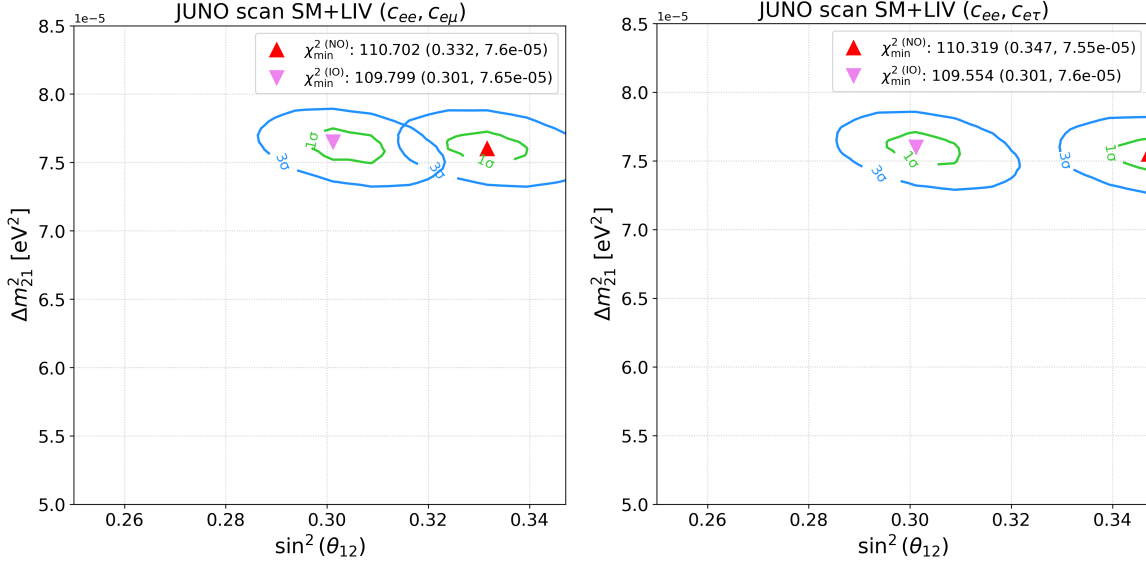


Figure 5: Sensitivity in the $\sin^2 \theta_{12} - \Delta m_{21}^2$ plane considering best-fit value of CP-violating parameters for $c_{ee}, c_{e\mu}$ (left) and $c_{ee}, c_{e\tau}$ (right). The 3σ and 1σ contours of NO and IO are shown by blue and green, respectively. Best fits are pointed by red and violet triangles for NO and IO, respectively.

The main observations from Figure 5 are,

- In both panels, the best-fit for NO (red triangle) shifts to a higher value of $\sin^2 \theta_{12} = 0.332$ (left), 0.347 (right). This shift separates it from the IO best-fit (violet triangle) of $\sin^2 \theta_{12} = 0.301$ by 3σ confidence due to the best-fit LIV parameters being included.
- The 3σ region of IO is similar to the standard case, but it yields a lower χ^2_{\min} in both cases. This indicates that JUNO data prefers IO even more when the best-fit LIV parameters are included.
- For the $(c_{ee}, c_{e\mu})$ case, the 3σ contours of NO and IO partially overlap. In contrast, in the presence of $(c_{ee}, c_{e\tau})$, the 3σ contours of NO are significantly distinct from IO.

We now shift our focus to CP-violating LIV parameters and determine their sensitivity. The CP-violating parameters, defined in (5) by $a_{\alpha\beta}$, are independent of neutrino energy and have dimension of energy. In Figure 6, we present the sensitivity in $a_{ee} - a_{e\mu}$ and $a_{ee} - a_{e\tau}$ channels respectively in left and right panels, while varying these parameters in the range of $(10^{-15}, 10^{-12})$. We can point out the followings

- The 3σ bounds are stronger for $a_{e\mu} \simeq 6.3 \times 10^{-13}$ GeV and $a_{e\tau} \simeq 7.2 \times 10^{-13}$ GeV than $a_{ee} \simeq 17 \times 10^{-13}$ GeV.
- The best-fit values in $a_{ee}, a_{e\mu}$ plane of $(10.0, 0.1) \times 10^{-13}$ GeV has $\chi^2_{\min} = 110.572$. In the other case, the best-fit in the $(a_{ee}, a_{e\tau})$ plane is $(12.60, 0.7) \times 10^{-13}$ GeV, which

corresponds to $\chi^2_{\min} = 110.473$. Both this χ^2 is lower than the standard 3ν fit of 110.750.

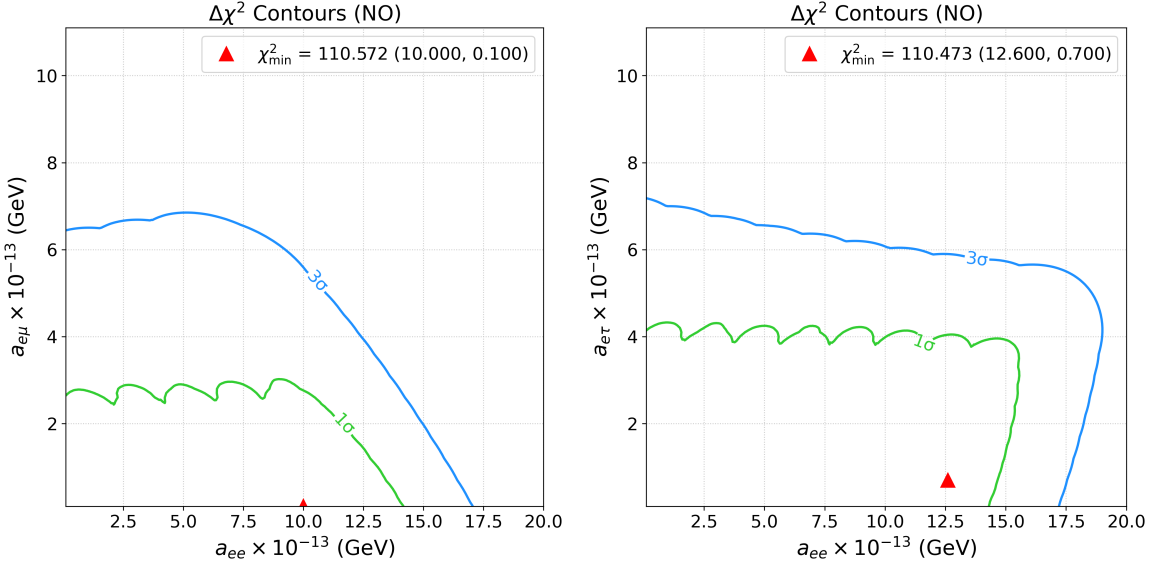


Figure 6: Two dimensional $\Delta\chi^2$ contours for the CP-violating parameter pairs $(a_{ee}, a_{e\mu})$ (left) and $(a_{ee}, a_{e\tau})$ (right) assuming normal ordering. The red triangles mark the global minima of each scan, which correspond to the best-fit LIV values preferred by the data. 1σ and 3σ contours are shown by green and blue lines, respectively.

Figure 7 depicts the sensitivity in $a_{e\mu} - \phi_{e\mu}$ and $a_{e\tau} - \phi_{e\tau}$ plane in the left and right panels, respectively. There are similar characteristics between Figure 7 and Figure 4. The observations are as follows,

- In both panels complete ranges of $\phi_{e\mu}, \phi_{e\tau}$ are allowed similar to CP-conserving case in Figure 4.
- Similar to Figure 4, around $\phi \simeq \pi/2, 3\pi/2$ values of phases, the sensitivity in the corresponding parameter decreases significantly, as shown by the horn-like structures.
- The best-fit points in both panels are distinct, unlike in Figure 4. For the left panel the best-fit is at $\phi_{e\mu} = 4.97, a_{e\mu} = 1.30 \times 10^{-13}$ GeV, whereas for right panel $\phi_{e\tau} = \pi, a_{e\tau} = 0.70 \times 10^{-13}$ GeV gives the best-fit. Also to be noted χ^2 at these points are less than the standard case.

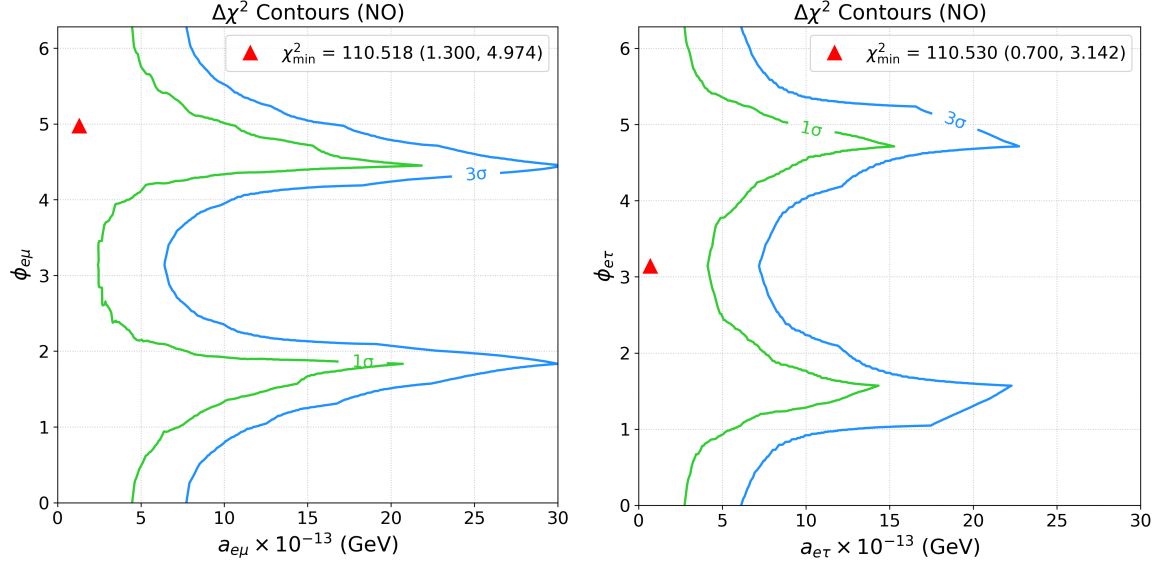


Figure 7: Two dimensional $\Delta\chi^2$ contours for the CP-violating parameter pairs $(a_{e\mu}, \phi_{e\mu})$ (left) and $(a_{e\tau}, \phi_{e\tau})$ (right) assuming normal ordering. The red triangles indicate the global minima of each scan, corresponding to the best-fit LIV values preferred by the data. 1σ and 3σ contours are shown by green and blue lines, respectively.

Plane	$a_{ee} - a_{e\mu}$	$a_{ee} - a_{e\tau}$	$a_{e\mu} - \phi_{e\mu}$	$a_{e\tau} - \phi_{e\tau}$
Best Fit	$(10.0, 0.1) \times 10^{-13}$ GeV	$(12.6, 0.7) \times 10^{-13}$ GeV	$(1.30 \times 10^{-13}$ GeV, 4.97)	$(0.70 \times 10^{-13}$ GeV, 3.14)
χ^2_{\min}	110.57	110.47	110.52	110.53
3σ	$(17.1, 6.8) \times 10^{-13}$ GeV	$(19.0, 7.1) \times 10^{-13}$ GeV	$(3.0 \times 10^{-12}$ GeV, N.A. ¹)	$(2.4 \times 10^{-12}$ GeV, N.A. ¹)

¹ The whole range is allowed.

Table 4: The best-fit values, χ^2_{\min} at the best-fit and 3σ bounds in our analysis (Fig. 6) for NO. A marginalization was performed on the parameter $\theta_{12}, \theta_{13}, \Delta m_{21}^2$ and Δm_{31}^2 .

Plane	$a_{ee} - a_{e\mu}$	$a_{ee} - a_{e\tau}$	$a_{e\mu} - \phi_{e\mu}$	$a_{e\tau} - \phi_{e\tau}$
Best Fit	$(1.5, 0.1) \times 10^{-13}$ GeV	$(0.1, 0.7) \times 10^{-13}$ GeV	$(1.30 \times 10^{-13}$ GeV, 1.05)	$(0.70 \times 10^{-13}$ GeV, 3.14)
χ^2_{\min}	109.61	109.38	109.40	109.37
3σ	$(17.0, 6.8) \times 10^{-13}$ GeV	$(18.9, 7.2) \times 10^{-13}$ GeV	$(2.3 \times 10^{-12}$ GeV, N.A. ¹)	$(2.3 \times 10^{-12}$ GeV, N.A. ¹)

¹ The whole range is allowed.

Table 5: The best fit values, χ^2_{\min} at the best fit and 3σ bounds in our analysis (Fig. 11) for IO. A marginalization was performed on the parameter $\theta_{12}, \theta_{13}, \Delta m_{21}^2$ and Δm_{31}^2 .

Now we use these best-fit values of CP-violating LIV coefficients as fixed inputs to generate JUNO+LIV sensitivity contours in the $\Delta m_{21}^2 - \sin^2 \theta_{12}$ plane, marginalizing over θ_{13} and Δm_{31}^2 within the ranges given in Table 1. Figure 8 shows these contours for both NO and IO, in the presence of the best-fit LIV parameters $(a_{ee}, a_{e\mu})$ (left panel) and $(a_{ee}, a_{e\tau})$ (right panel).

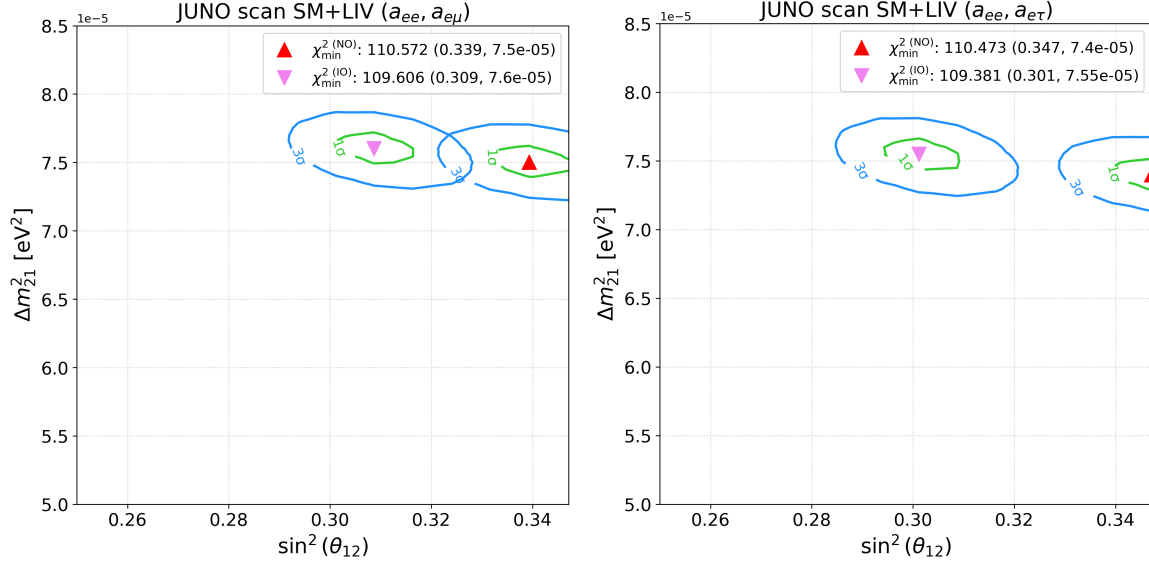


Figure 8: Sensitivity in the $\sin^2 \theta_{12} - \Delta m_{21}^2$ plane considering best-fit value of CP-violating parameters for $a_{ee}, a_{e\mu}$ (left) and $a_{ee}, a_{e\tau}$ (right). The 3σ and 1σ contours of NO and IO are shown by blue and green, respectively. Best fit are pointed by red and violet triangles for NO and IO, respectively.

Similar to CP-conserving cases (Figure 5), we obtained also preference for inverted ordering. The main observations from Figure 8 are,

- The best-fit for NO (red triangle) moves to a higher value of $\sin^2 \theta_{12} = 0.339$ (left), 0.347 (right), separating from the IO best-fit (violet triangle) by 3σ .
- The 3σ regions of IO are similar to the region obtained in the standard case and they cover the standard best-fits also.
- For the $(a_{ee}, a_{e\mu})$ case, the 3σ contours of NO and IO partially overlap, but in case of $(a_{ee}, a_{e\tau})$, the 3σ contours of NO, IO are separated comfortably.

5 Conclusion

We investigate the potential of the JUNO experiment to search for LIV through reactor antineutrino oscillations. Working in an extension of the SM, we included both CPT-even and CPT-odd LIV coefficients in the effective neutrino Hamiltonian to assess how these parameters modify the oscillation pattern in the JUNO experiment.

A complete simulation and statistical analysis were performed using the 59.1-day data release [2]. We employed a GLoBES framework, generating oscillated event spectra across 64 prompt energy bins [1, 9] MeV for a 52.5 km baseline, incorporating a 3% energy resolution. Our analysis used a Poissonian χ^2 statistic with pull terms, marginalizing over the standard oscillation parameters (θ_{12} , θ_{13} , Δm_{21}^2 , Δm_{31}^2) within their current experimental ranges. We first validated our setup by reproducing the JUNO collaboration’s $\sin^2 \theta_{12} - \Delta m_{21}^2$ sensitivity contours for standard oscillations.

Numerically, we derive competitive constraints on the LIV coefficients from this initial dataset. For CPT-odd (CP-violating) parameters, the 3σ limits are $a_{ee} \lesssim 2.2 \times 10^{-12}$ GeV, $a_{e\mu} \lesssim 8.0 \times 10^{-13}$ GeV, and $a_{e\tau} \lesssim 6 \times 10^{-13}$ GeV. For the CPT-even (CP-conserving) sector, we find $c_{ee} \lesssim 1.0 \times 10^{-18}$, $c_{e\tau} \lesssim 2.7 \times 10^{-19}$ GeV, and $c_{e\mu} \lesssim 2 \times 10^{-19}$ GeV. The phases don’t have enough sensitivity themselves, but they affect the sensitivity of their corresponding partners at around $\pi/2$ and $3\pi/2$. All numerical results are listed in Tables 2–5.

Our analysis reveals that including the best-fit LIV parameters, obtained from our analysis, significantly reshapes the inferred oscillation parameter space. The normal ordering best-fit points shift to higher values of the solar angle θ_{12} , in the c_{ee} – $c_{e\tau}$ scenario. This shift creates a separation of approximately 3σ from the inverted ordering best-fit, which remains near the standard value. Crucially, the inverted ordering scenario consistently provides a better fit to data, yielding a lower χ^2_{\min} and demonstrating a clear 3σ preference when LIV effects are included.

This study finds that including best-fit LIV parameters in the oscillation fit yields a 3σ preference for inverted over normal mass ordering in the $\sin^2 \theta_{12} - \Delta m_{21}^2$ parameter space. This modified mass ordering preference may reshape current degeneracies in global neutrino fits. The observed parameter-space reshuffling, combined with the stringent bounds reported here, highlights JUNO’s emerging capability to test fundamental physics. With larger future datasets, JUNO should substantially enhance sensitivity to both Lorentz violation and the neutrino mass ordering.

Acknowledgments

Work supported by ANID-Chile under the grant FONDECYT Regular No. 1241855. T.A. thanks the support from ANID-Chile through the National Doctoral Fellowship No. 21250478. S.P. acknowledges the funding from ANID-Chile under FONDECYT Postdoctorado No. 3250376.

A Results for Inverted Ordering

As we mentioned in Section 4, the results for the inverted ordering case are almost similar to the NO. Figure 9, with contours similar to Figure 3, shows the best-fit obtained at $(c_{ee}, c_{e\mu}) \simeq (0.01, 0.01) \times 10^{-19}$ with $\chi^2 = 109.799$, and $(c_{ee}, c_{e\tau}) \simeq (0.01, 0.05) \times 10^{-19}$ with $\chi^2 = 109.554$, less compared to standard $\chi^2_{\min} = 109.751$. The contours and best-fits in Figure 10 in $(c_{e\mu}, \phi_{e\mu})$ and $(c_{e\tau}, \phi_{e\tau})$ for IO are mostly identical to Figure 4.

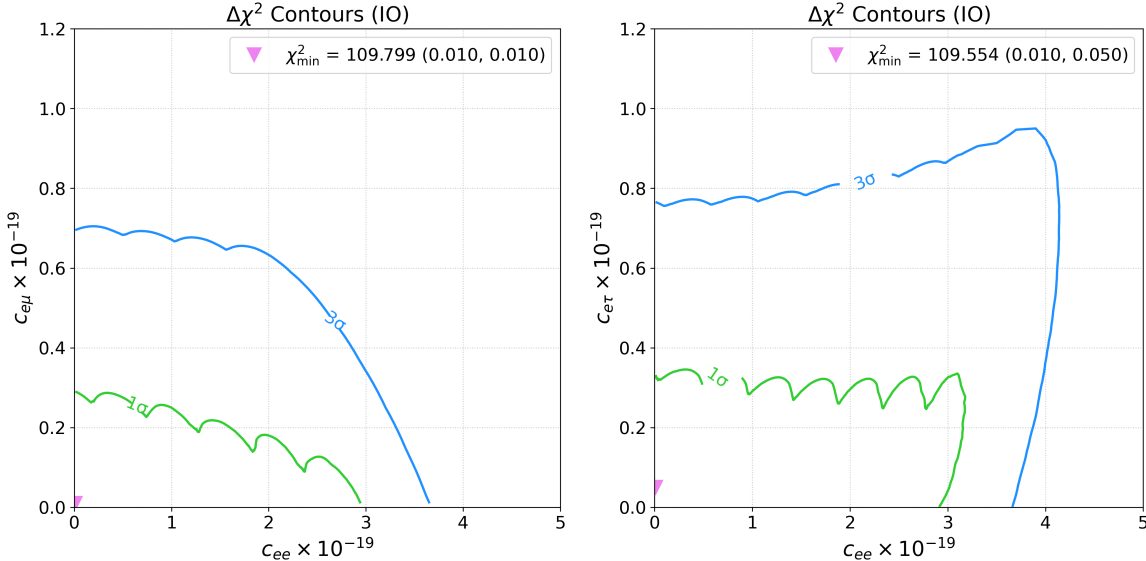


Figure 9: Two dimensional $\Delta\chi^2$ contours for the LIV parameter pairs $(c_{ee}, c_{e\mu})$ (left) and $(c_{ee}, c_{e\tau})$ (right) assuming inverted ordering. The red triangles mark the global minima of each scan, which correspond to the best-fit LIV values preferred by the data. 1σ and 3σ contours are shown by green and blue lines, respectively.

For CP-violating cases, the 3σ region in Figure 11 for IO is almost similar to the NO case (Figure 6). The best-fit is obtained at $(a_{ee}, a_{e\mu}) \simeq (1.5, 0.1) \times 10^{-13}$ GeV with $\chi^2 = 109.606$, and $(a_{ee}, a_{e\tau}) \simeq (0.1, 0.7) \times 10^{-13}$ GeV with $\chi^2 = 109.381$, less compared to standard $\chi^2_{\min} = 109.751$. The contours and best-fits in the $(a_{e\tau}, \phi_{e\tau})$ plane, right panels of Figure 12 for IO and Figure 7 for NO are mostly identical. However, in the case of IO, the $a_{e\mu}$ is a slightly better constraint than NO in the $(a_{e\mu}, \phi_{e\mu})$ plane as seen from the left panels of Figure 12 and Figure 7.

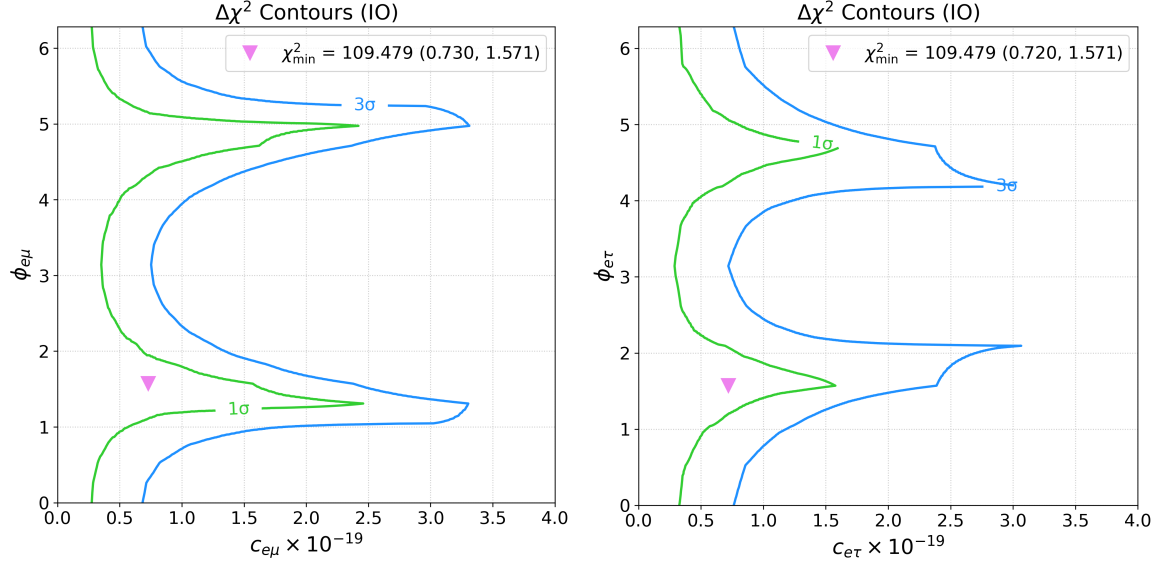


Figure 10: Two dimensional $\Delta\chi^2$ contours for the LIV parameter pairs $(c_{e\mu}, \phi_{e\mu})$ (left) and $(c_{e\tau}, \phi_{e\tau})$ (right) assuming inverted ordering. The red triangles mark the global minima of each scan, which correspond to the best-fit LIV values preferred by the data. 1σ and 3σ contours are shown by green and blue lines, respectively.

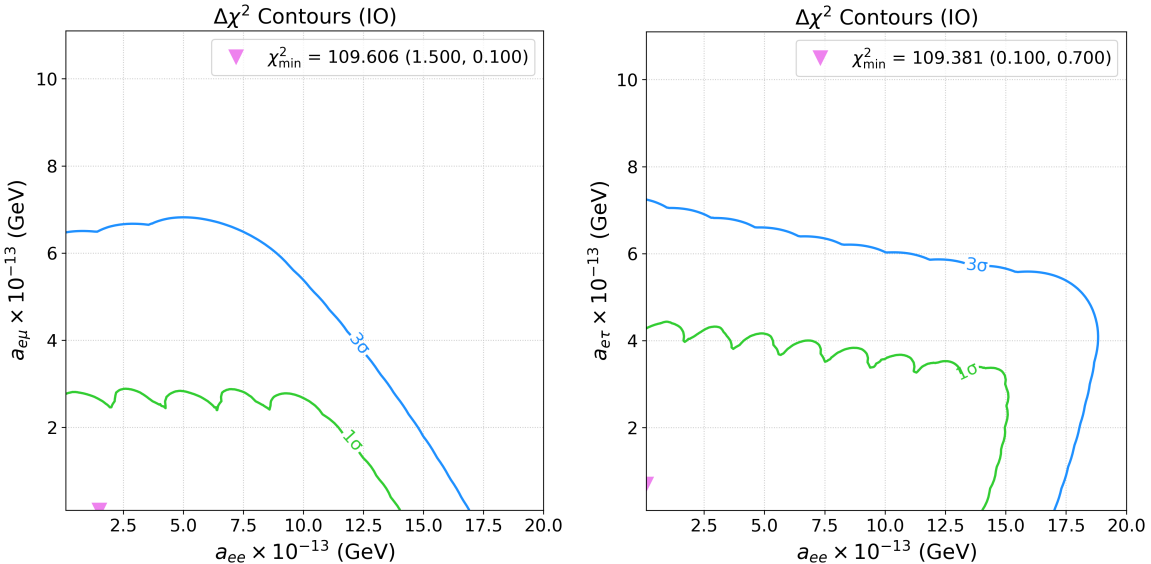


Figure 11: Two dimensional $\Delta\chi^2$ contours for the CP-violating parameter pairs $(a_{ee}, a_{e\mu})$ (left) and $(a_{ee}, a_{e\tau})$ (right) assuming inverted ordering. The red triangles mark the global minima of each scan, which correspond to the best-fit LIV values preferred by the data. 1σ and 3σ contours are shown by green and blue lines, respectively.

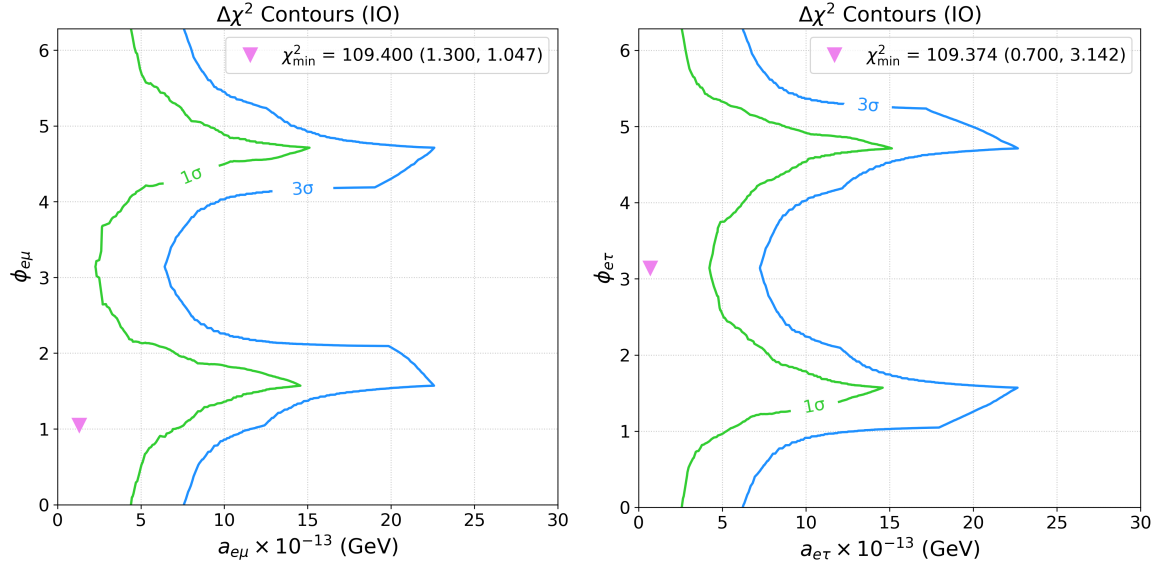


Figure 12: Two dimensional $\Delta\chi^2$ contours for the CP-violating parameter pairs $(a_{e\mu}, \phi_{e\mu})$ (left) and $(a_{e\tau}, \phi_{e\tau})$ (right) assuming inverted ordering. The red triangles mark the global minima of each scan, which correspond to the best-fit LIV values preferred by the data. 1σ and 3σ contours are shown by green and blue lines, respectively.

References

- [1] S. Navas et al. “Review of Particle Physics”. In: *Phys. Rev. D* 110 (3 Aug. 2024), p. 030001. DOI: [10.1103/PhysRevD.110.030001](https://doi.org/10.1103/PhysRevD.110.030001). URL: <https://link.aps.org/doi/10.1103/PhysRevD.110.030001>.
- [2] Angel Abusleme et al. “First measurement of reactor neutrino oscillations at JUNO”. In: *arXiv preprint arXiv:2511.14593* (2025).
- [3] Rudra Majhi, Soumya Chembra, and Rukmani Mohanta. “Exploring the effect of Lorentz invariance violation with the currently running long-baseline experiments”. In: *Eur. Phys. J. C* 80.5 (2020), p. 364. DOI: [10.1140/epjc/s10052-020-7963-1](https://doi.org/10.1140/epjc/s10052-020-7963-1). arXiv: [1907.09145 \[hep-ph\]](https://arxiv.org/abs/1907.09145).
- [4] Sanjib Kumar Agarwalla and Mehedi Masud. “Can Lorentz invariance violation affect the sensitivity of deep underground neutrino experiment?” In: *Eur. Phys. J. C* 80.8 (2020), p. 716. DOI: [10.1140/epjc/s10052-020-8303-1](https://doi.org/10.1140/epjc/s10052-020-8303-1). arXiv: [1912.13306 \[hep-ph\]](https://arxiv.org/abs/1912.13306).
- [5] Ushak Rahaman. “Looking for Lorentz invariance violation (LIV) in the latest long baseline accelerator neutrino oscillation data”. In: *Eur. Phys. J. C* 81.9 (2021), p. 792. DOI: [10.1140/epjc/s10052-021-09598-4](https://doi.org/10.1140/epjc/s10052-021-09598-4). arXiv: [2103.04576 \[hep-ph\]](https://arxiv.org/abs/2103.04576).
- [6] Rudra Majhi et al. “Distinguishing nonstandard interaction and Lorentz invariance violation at the Protvino to super-ORCA experiment”. In: *Phys. Rev. D* 107.7 (2023), p. 075036. DOI: [10.1103/PhysRevD.107.075036](https://doi.org/10.1103/PhysRevD.107.075036). arXiv: [2212.07244 \[hep-ph\]](https://arxiv.org/abs/2212.07244).
- [7] Nishat Fiza, Nafis Rezwan Khan Chowdhury, and Mehedi Masud. “Investigating Lorentz Invariance Violation with the long baseline experiment P2O”. In: *JHEP* 01 (2023), p. 076. DOI: [10.1007/JHEP01\(2023\)076](https://doi.org/10.1007/JHEP01(2023)076). arXiv: [2206.14018 \[hep-ph\]](https://arxiv.org/abs/2206.14018).
- [8] Supriya Pan, Kaustav Chakraborty, and Sribabati Goswami. “Sensitivity to CP discovery in the presence of Lorentz invariance-violating potential at T2HK/T2HKK”. In: *Eur. Phys. J. C* 84.4 (2024), p. 354. DOI: [10.1140/epjc/s10052-024-12541-y](https://doi.org/10.1140/epjc/s10052-024-12541-y). arXiv: [2308.07566 \[hep-ph\]](https://arxiv.org/abs/2308.07566).
- [9] Luis A. Delgado et al. “Constraining the isotropic CPT-odd coefficients of the standard model extension by a combined DUNE and ESSnuSB analysis”. In: *Phys. Rev. D* 111.9 (2025), p. 095027. DOI: [10.1103/PhysRevD.111.095027](https://doi.org/10.1103/PhysRevD.111.095027). arXiv: [2409.03716 \[hep-ph\]](https://arxiv.org/abs/2409.03716).
- [10] Rubén Cordero et al. “Neutrino Lorentz invariance violation from the *CPT*-even SME coefficients through a tensor interaction with cosmological scalar fields”. In: *Eur. Phys. J. C* 85.1 (2025), p. 6. DOI: [10.1140/epjc/s10052-024-13719-0](https://doi.org/10.1140/epjc/s10052-024-13719-0). arXiv: [2407.18513 \[hep-ph\]](https://arxiv.org/abs/2407.18513).
- [11] Himanshu Bora, Debjyoti Dutta, and Abinash Medhi. “Constraining and Resolving Lorentz-Violating New Physics at ESSnuSB Using Complementarity with DUNE”. In: (Dec. 2025). arXiv: [2512.06953 \[hep-ph\]](https://arxiv.org/abs/2512.06953).
- [12] Deepak Raikwal, Sandhya Choubey, and Monojit Ghosh. “Comprehensive study of LIV in atmospheric and long-baseline experiments”. In: (Mar. 2023). arXiv: [2303.10892 \[hep-ph\]](https://arxiv.org/abs/2303.10892).

[13] Lukas Hennig, Alba Domi, and Carlos Argüelles-Delgado. “Combined search for Lorentz invariance violation with ANTARES, IceCube, and KM3NeT”. In: *PoS* ICRC2025 (2025), p. 1058. DOI: [10.22323/1.501.1058](https://doi.org/10.22323/1.501.1058).

[14] B. Aharmim et al. “Tests of Lorentz invariance at the Sudbury Neutrino Observatory”. In: *Phys. Rev. D* 98.11 (2018), p. 112013. DOI: [10.1103/PhysRevD.98.112013](https://doi.org/10.1103/PhysRevD.98.112013). arXiv: [1811.00166 \[hep-ex\]](https://arxiv.org/abs/1811.00166).

[15] Hai-Xing Lin, Jie Ren, and Jian Tang. “Anisotropic Lorentz invariance violation in reactor neutrino experiments”. In: *Front. Phys. (Beijing)* 21.1 (2026), p. 16200. DOI: [10.15302/frontphys.2026.016200](https://doi.org/10.15302/frontphys.2026.016200). arXiv: [2503.02305 \[hep-ph\]](https://arxiv.org/abs/2503.02305).

[16] Paolo Walter Cattaneo. “Constraints on Lorentz invariance from the event KM3-230213A”. In: *Eur. Phys. J. C* 85.5 (2025), p. 529. DOI: [10.1140/epjc/s10052-025-14264-0](https://doi.org/10.1140/epjc/s10052-025-14264-0). arXiv: [2502.13201 \[hep-ph\]](https://arxiv.org/abs/2502.13201).

[17] Yu-Ming Yang et al. “Constraints on Lorentz-invariance violation in the neutrino sector from the ultrahigh-energy event KM3-230213A”. In: *Phys. Rev. D* 111.12 (2025), p. 123037. DOI: [10.1103/6zzg-tv4s](https://doi.org/10.1103/6zzg-tv4s). arXiv: [2502.18256 \[hep-ph\]](https://arxiv.org/abs/2502.18256).

[18] Petr Satunin. “Ultra-high-energy event KM3-230213A constraints on Lorentz Invariance Violation in neutrino sector”. In: *Eur. Phys. J. C* 85.5 (2025), p. 545. DOI: [10.1140/epjc/s10052-025-14240-8](https://doi.org/10.1140/epjc/s10052-025-14240-8). arXiv: [2502.09548 \[hep-ph\]](https://arxiv.org/abs/2502.09548).

[19] J. B. Albert et al. “First Search for Lorentz and CPT Violation in Double Beta Decay with EXO-200”. In: *Phys. Rev. D* 93.7 (2016), p. 072001. DOI: [10.1103/PhysRevD.93.072001](https://doi.org/10.1103/PhysRevD.93.072001). arXiv: [1601.07266 \[nucl-ex\]](https://arxiv.org/abs/1601.07266).

[20] M. Aker et al. “Search for Lorentz-invariance violation with the first KATRIN data”. In: *Phys. Rev. D* 107.8 (2023), p. 082005. DOI: [10.1103/PhysRevD.107.082005](https://doi.org/10.1103/PhysRevD.107.082005). arXiv: [2207.06326 \[nucl-ex\]](https://arxiv.org/abs/2207.06326).

[21] V. Alan Kostelecký and Matthew Mewes. “Lorentz and CPT violation in neutrinos”. In: *Phys. Rev. D* 69 (1 Jan. 2004), p. 016005. DOI: [10.1103/PhysRevD.69.016005](https://doi.org/10.1103/PhysRevD.69.016005).

[22] D. Colladay and V. Alan Kostelecký. “Lorentz-violating extension of the standard model”. In: *Phys. Rev. D* 58 (11 Oct. 1998), p. 116002. DOI: [10.1103/PhysRevD.58.116002](https://doi.org/10.1103/PhysRevD.58.116002). URL: <https://link.aps.org/doi/10.1103/PhysRevD.58.116002>.

[23] V. Alan Kostelecký and Matthew Mewes. “Lorentz and CPT violation in the neutrino sector”. In: *Phys. Rev. D* 70 (3 Aug. 2004), p. 031902. DOI: [10.1103/PhysRevD.70.031902](https://doi.org/10.1103/PhysRevD.70.031902). URL: <https://link.aps.org/doi/10.1103/PhysRevD.70.031902>.

[24] Gabriela Barenboim. “Some Aspects About Pushing the CPT and Lorentz Invariance Frontier With Neutrinos”. In: *Frontiers in Physics* 10, 813753 (May 2022), p. 813753. DOI: [10.3389/fphy.2022.813753](https://doi.org/10.3389/fphy.2022.813753).

[25] Matthias Raphael Stock and on behalf of the JUNO collaboration. “Status and prospects of the JUNO experiment”. In: *SciPost Phys. Proc.* (2025), p. 020. DOI: [10.21468/SciPostPhysProc.17.020](https://doi.org/10.21468/SciPostPhysProc.17.020).

- [26] P. Huber, M. Lindner, and W. Winter. “Simulation of long-baseline neutrino oscillation experiments with GLoBES”. In: *Computer Physics Communications* 167.3 (May 2005), pp. 195–202. ISSN: 0010-4655. DOI: [10.1016/j.cpc.2005.01.003](https://doi.org/10.1016/j.cpc.2005.01.003). URL: <http://dx.doi.org/10.1016/j.cpc.2005.01.003>.
- [27] Patrick Huber et al. “New features in the simulation of neutrino oscillation experiments with GLoBES 3.0”. In: *Computer Physics Communications* 177.5 (Sept. 2007), pp. 432–438. ISSN: 0010-4655. DOI: [10.1016/j.cpc.2007.05.004](https://doi.org/10.1016/j.cpc.2007.05.004). URL: <http://dx.doi.org/10.1016/j.cpc.2007.05.004>.
- [28] Joachim Kopp. *Sterile neutrinos and non-standard neutrino interactions in GLoBES (snu-1.0)*. Technical Report / Software Manual. Version v1.0. Available online: snu-1.0 code manual; implementation for sterile neutrinos and NSI in GLoBES. Max Planck Institute for Physics (Munich), Nov. 2010. URL: <https://www.xn--mpihd-ou3b.mpg.de/personalhomes/globes/tools/snu-1.0.pdf>.
- [29] F. P. An et al. “Precision Measurement of Reactor Antineutrino Oscillation at Kilometer-Scale Baselines by Daya Bay”. In: *Phys. Rev. Lett.* 130 (16 Apr. 2023), p. 161802. DOI: [10.1103/PhysRevLett.130.161802](https://doi.org/10.1103/PhysRevLett.130.161802). URL: <https://link.aps.org/doi/10.1103/PhysRevLett.130.161802>.